ELSEVIER

International Journal of Heat and Fluid Flow 22 (2001) 332–342

International Journal of HEAT AND FLUID FLOW

www.elsevier.com/locate/ijhff

Direct numerical simulation of turbulent Couette flow with immiscible droplets

Toshihiko Iwasaki, Koji Nishimura [1], Mitsuru Tanaka, Yoshimichi Hagiwara *

Department of Mechanical and System Engineering, Kyoto Institute of Technology, Sakyo-ku, Goshokaido-cho, Matsugasaki, Kyoto 606-8585, Japan

Abstract

A direct numerical simulation has been carried out in order to clarify the effects of the high viscosity and the interfacial tension of a droplet on the interaction between the droplet and near-wall turbulence. A liquid turbulent plane Couette flow with an immiscible droplet of the same fluid density as that of the continuous-phase has been used. The diameter of the droplet is fixed at one-fourth of the wall distance, which is nearly equal to 41 wall units. The droplet has been assigned in the range of 20–60 wall units from one moving wall initially. The modified volume of fluid (VOF) algorithm and local grid refinement are used for tracking the phase interface. The velocities for the fine grid are decided so that the equation of continuity is satisfied in the fine cell. It is found that the deformation of the droplet due to the surrounding fluid flow is suppressed by the effect of the interfacial tension of the droplet. The streamwise vortex is attenuated by the existence of the droplet with the interfacial tension. The small vortex is generated in the wake region of the droplet. The Reynolds-shear stress product becomes higher in a wide region around the droplet. © 2001 Elsevier Science Inc. All rights reserved.

Keywords: Shear-dominant flow; Immiscible droplets; Turbulence modification; Coherent structure; Direct numerical simulation

1. Introduction

Liquid–liquid two-phase dispersed flows are the primary phenomena in engineering applications such as direct-contact heat exchangers. The control of the flows is expected to contribute to an efficient use of energy. Also, it was reported that immiscible droplets are effective for drag reduction for turbulent liquid flows in pipes (Pal, 1993; Angeli and Hewitt, 1998). However, the structures and the dynamics of the flows have not been well understood owing to the complexity of the interaction between the deformable droplets and the surrounding fluid flow.

In order to clarify such interaction, our research group has focused on interaction between droplets and surrounding turbulence. We found that the droplet deformation and the flow induced by the droplet depend on whether the droplet is located near shear-dominant turbulence, strain-dominant turbulence or eddy-dominant turbulence (Hagiwara et al., 1997a). Attention was then focused on shear-dominant flows, which not only have the capability to deform droplets but also play an essential role in the production of turbulence energy. We also examined the interaction between a turbulent plane Couette flow and a high-viscosity immiscible droplet without the interfacial tension located at the center of the flow and found that the droplet attenuated a streamwise vortex locally (Hagiwara et al., 1997b). In this paper, the modified volume of fluid (VOF) algorithm and local grid refinement were adopted for tracking the phase interface. Although other methods, such as the front-tracking method (Unverdi and Tryggivason, 1992) and the level set method (Osher and Sethian, 1988) may be applicable, they have not been fully adopted to the prediction of bubbles or droplets in turbulent flow.

In the present study, a droplet is set near a wall, then the deformation of the droplet with and without interfacial tension are examined by direct numerical simulation using local grid refinement. In the calculation of interfacial tension, we adopt the method based on a spherical surface estimated from the fraction of carrier fluid for fine cubic cells (Tanaka et al., 1997). The first and the second derivatives of height functions from the reference planes (i.e., the surfaces of computational domain) to the interface can be applicable for estimating the radius of curvature (Tomiyama et al., 1995). However, the height function has a relatively large error for the interface in the 'middle latitude' compared with that for the interface near the 'poles' or the 'equator' of the spherical droplet, and the noticeable deformations of the droplet due to the mean velocity profile occur near the 'middle latitude'. The continuum surface force (CSF) model is also promising for the prediction of the interfacial tension (Brackbill et al., 1992). In this method, the transition region with finite thickness is

* Corresponding author. Tel.: +81-75-724-7324; fax: +81-75-724-7300.

E-mail addresses: mtanaka@ipc.kit.ac.jp (M. Tanaka), yoshi@ipc.kit.ac.jp (Y. Hagiwara).

[1] Present address: TCM Co. Ltd., Ryugasaki, Ibaraki Pref. 301-8501, Japan.

0142-727X/01/$ - see front matter © 2001 Elsevier Science Inc. All rights reserved.
PII: S0142-727X(01)00096-0

Notation

C	center for spherical interface
Ct	Courant number
F	fraction of continuous-phase fluid
$\bar{F}$	average value of F over domain
f	external body force per unit mass
h	half of the wall distance
I_x, I_y, I_z	number of grid points
K_f	mean kinetic energy per unit mass of carrier fluid flow ($=\frac{1}{2}U^2$)
K_s	surface tension energy
L_x, L_z	size of computational domain
M	total number of points of intersection between spherical surface and sides of cell
N	points of intersection between spherical surface and side of cell
$\boldsymbol{n}$	unit vector normal to the interface
p	pressure
R	radius of a spherical interface
Re	Reynolds number
S	interface area
t	time
U	streamwise mean velocity
U_W	constant speed of moving wall
u, v, w	velocities in the streamwise, wall-normal and transverse directions
u', v', w'	fluctuating velocity components
$u'_{rms}, v'_{rms}, w'_{rms}$	root-mean-square of fluctuating velocity components
u_τ	friction velocity
$-\overline{u'v'}$	Reynolds shear stress
$-u'v'$	Reynolds-shear stress product
x, y, z	axes in the streamwise, wall-normal and transverse directions

Greeks

Δx	grid spacing in the x direction
$\Delta\tilde{x}$	dimension of fine cubic cell
$\Delta y(y)$	grid spacing in the y direction
Δz	grid spacing in the z direction
μ_c	viscosity of continuous-phase fluid
μ_d	viscosity of dispersed-phase fluid
ν	kinematic viscosity
ρ	density
σ	surface tension coefficient
τ	viscous stress
ω	vorticity

Superscripts and subscript

$()^+$	value made dimensionless with the wall parameters u_τ and ν
$()^*$	value made dimensionless with U_W and h
$\tilde{()}$	value for fine cubic cell
$()_m$	point for the intersection

considered at any time step. However, the effect of transition region on near-interface turbulence has not yet been validated. Therefore, we do not apply these two methods. The effects of the droplets on streamwise vortices in near-wall turbulence are examined.

2. Computational procedures

2.1. Configuration

We considered a turbulent flow, realized between two parallel walls at a distance of $2h$ moving in opposite directions with a constant speed of U_W (see Fig. 1), with immiscible droplets between the walls. The x-, y- and z- axes were assigned as in the direction of flow, normal to the wall and along the transverse direction to the flow, respectively. The origin of the coordinate was set at the center of the rectangular computational domain of the sides of $8h \times 2h \times 4h$. The computational domain was divided into $64 \times 50 \times 64$ rectangular cells of the sides of $\Delta x \times \Delta y(y) \times \Delta z$. The cell dimension was set to be uniform in the x and z directions, but non-uniform in the y direction. We took $\Delta y(y)$ as $\Delta y(y) = \Delta z = \Delta x/2$ for $|y/h| \leqslant 0.75$ in the central core region, $\Delta y(y) = \Delta y(0)/2$ for $0.75 \leqslant |y/h| \leqslant 0.875$, $\Delta y(y) = \Delta y(0)/4$ for $0.875 \leqslant |y/h| \leqslant 0.992$, and $\Delta y(y) = \Delta y(0)/8$ for $0.992 \leqslant |y/h| \leqslant 1$ in near-wall regions. These dimensions are suitable for grid refinement mentioned in Section 2.3 in each cell. In the present study, we set the Reynolds number Re^* based on U_W and h at 1300. The Reynolds number, Re^+, based on the friction velocity, u_τ, was 82.6, so that the streamwise cell dimension was 10.36 in the wall unit. In Table 1, the domain size (L_x, L_z), the number of grid points (I_x, I_y, I_z), the grid spacing, and the Reynolds numbers are compared with those adopted in direct numerical simulations for Couette flows without droplets done by Papavassiliou and Hanratty (1997), Bech et al. (1995), Hamilton et al. (1995) and Lee and Kim (1991).

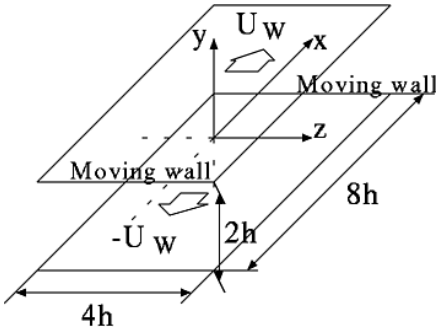

Fig. 1. Computational domain.

The fluid density of the droplet was assumed to be the same as that of the continuous-phase, and we focused on the effects of the viscosity and the interfacial tension of the droplet on the phase interaction.

2.2. Basic equations

The motion of the viscous incompressible fluid with constant mass density is described by the Navier–Stokes equation

$$\frac{\partial u_i}{\partial t} = -u_k \frac{\partial u_i}{\partial x_k} - \frac{\partial p}{\partial x_i} + \frac{\partial \tau_{ij}}{\partial x_i} + f_i \tag{1}$$

supplemented by the continuity equation $\partial u_k/\partial x_h = 0$, where

$$\tau_{ij} = \mu(\boldsymbol{x})\left(\frac{\partial u_i}{\partial x_j} + \frac{\partial u_j}{\partial x_i}\right) \tag{2}$$

and $\boldsymbol{x} = (x_1, x_2, x_3) = (x, y, z)$. Here, $(u_1, u_2, u_3) = (u, v, w)$, p, μ, τ_{ij} are the instant velocity, the pressure, the viscous

Table 1
Dimensions of computational domain and grid arrangement[a]

Case	L_x/h	L_z/h	I_x	I_y	I_z	xu_τ/v	yu_τ/v zu_τ/v	$Re^* = U_W h/v$		$Re^+ = u_\tau h/v$
With droplet										
Present	8.0	4.0	64	50	64	10.4	0.65, 1.3, 2.59, 5.18	5.18	1300	82.6
Hagiwara et al. (1997b)	4.0	4.0	64	44	64	5.28	0.75–5.28	5.28	1300	84.6
Without droplet										
Papavassiliou and Hanratty (1997)	4π	2π	128	65	64	14.7	NA	7.36	2660	150
Bech et al. (1995)	10π	4π	256	70	256	10.1	0.70–3.94	4.0	1300	82.2
Hamilton et al. (1995)	1.75π	1.2π	16	33	16	[11.9]	[0.17–3.4]	[8.2]	400	33
Lee and Kim (1991)	4π	2.7π	192	129	288	11.1	0.20–6.4	4.9	3000	170

[a] [ ] indicates the average of time-varying values due to u_τ fluctuations.

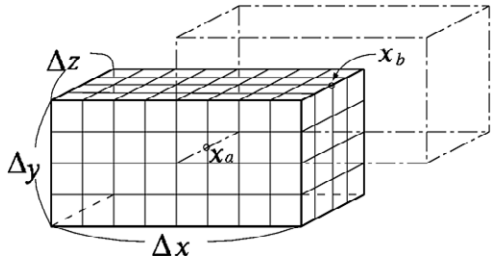

Fig. 2. Evaluation of viscous coefficient.

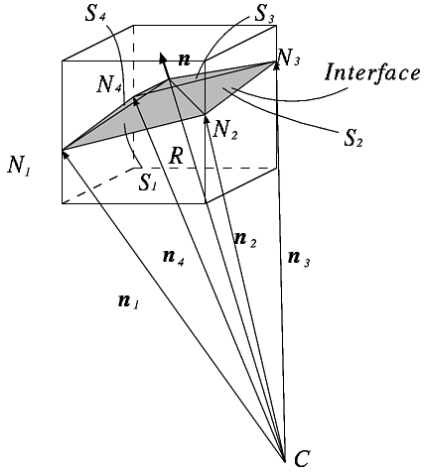

Fig. 3. Normal vector and interface area.

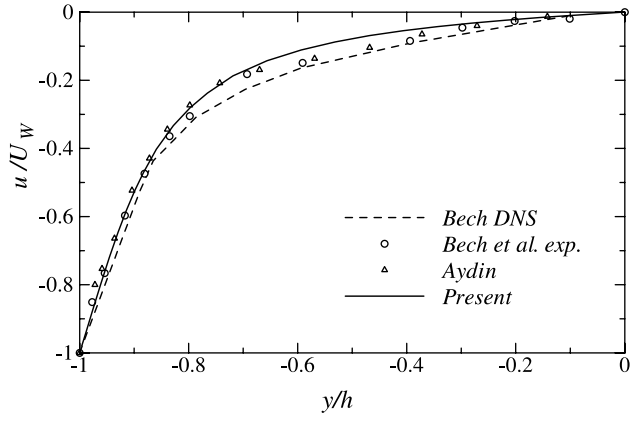

Fig. 4. Mean velocity profile in the case without droplet.

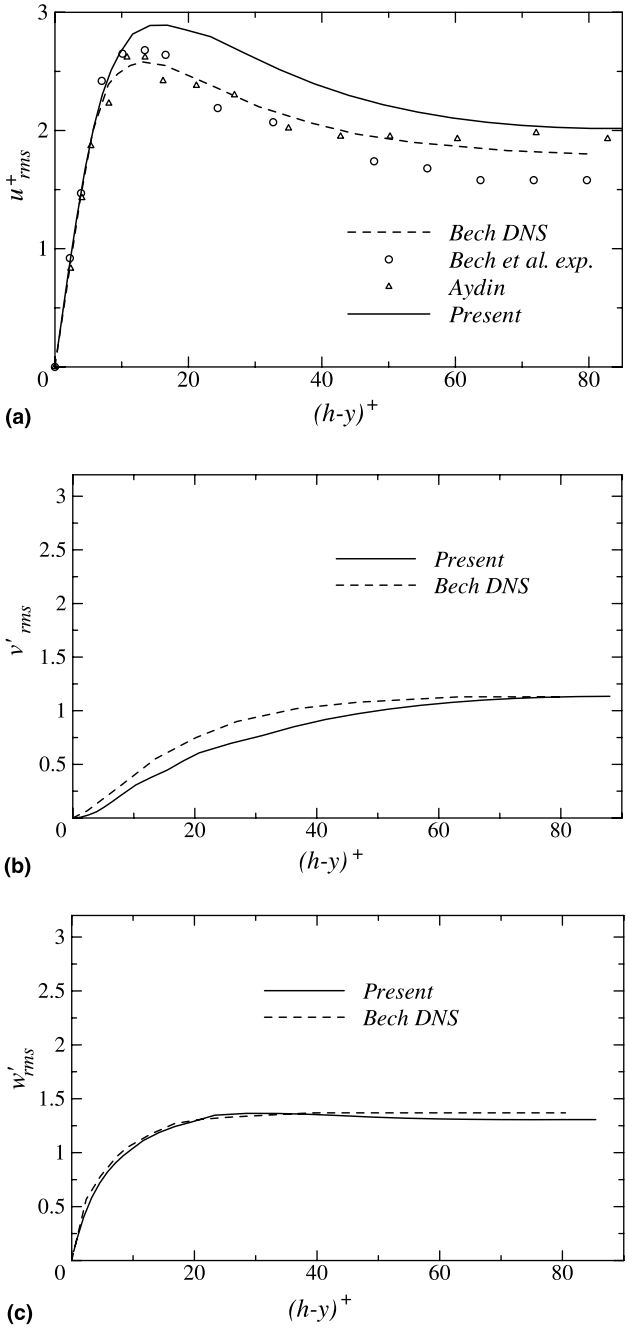

Fig. 5. Turbulence intensities in the case without droplet: (a) $u'_{\rm rms}$, (b) $v'_{\rm rms}$, (c) $w'_{\rm rms}$.

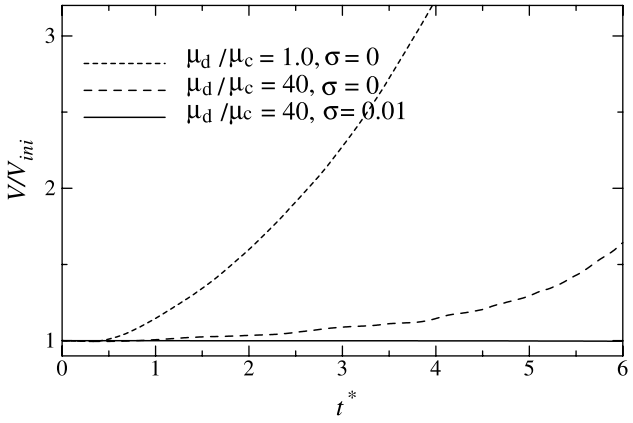

Fig. 6. Time changes in droplet volume.

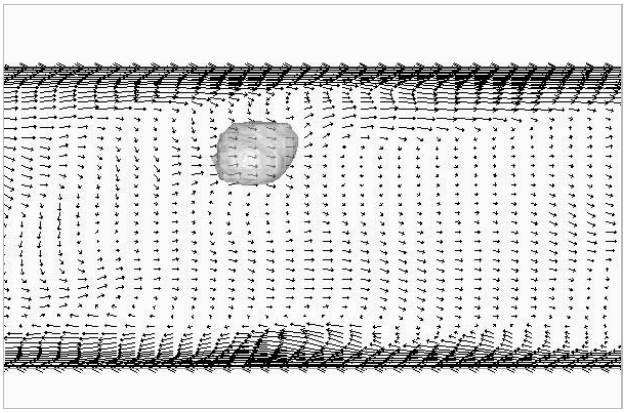

Fig. 7. Snapshot of velocity vectors on a (x, z)-plane near the droplet center.

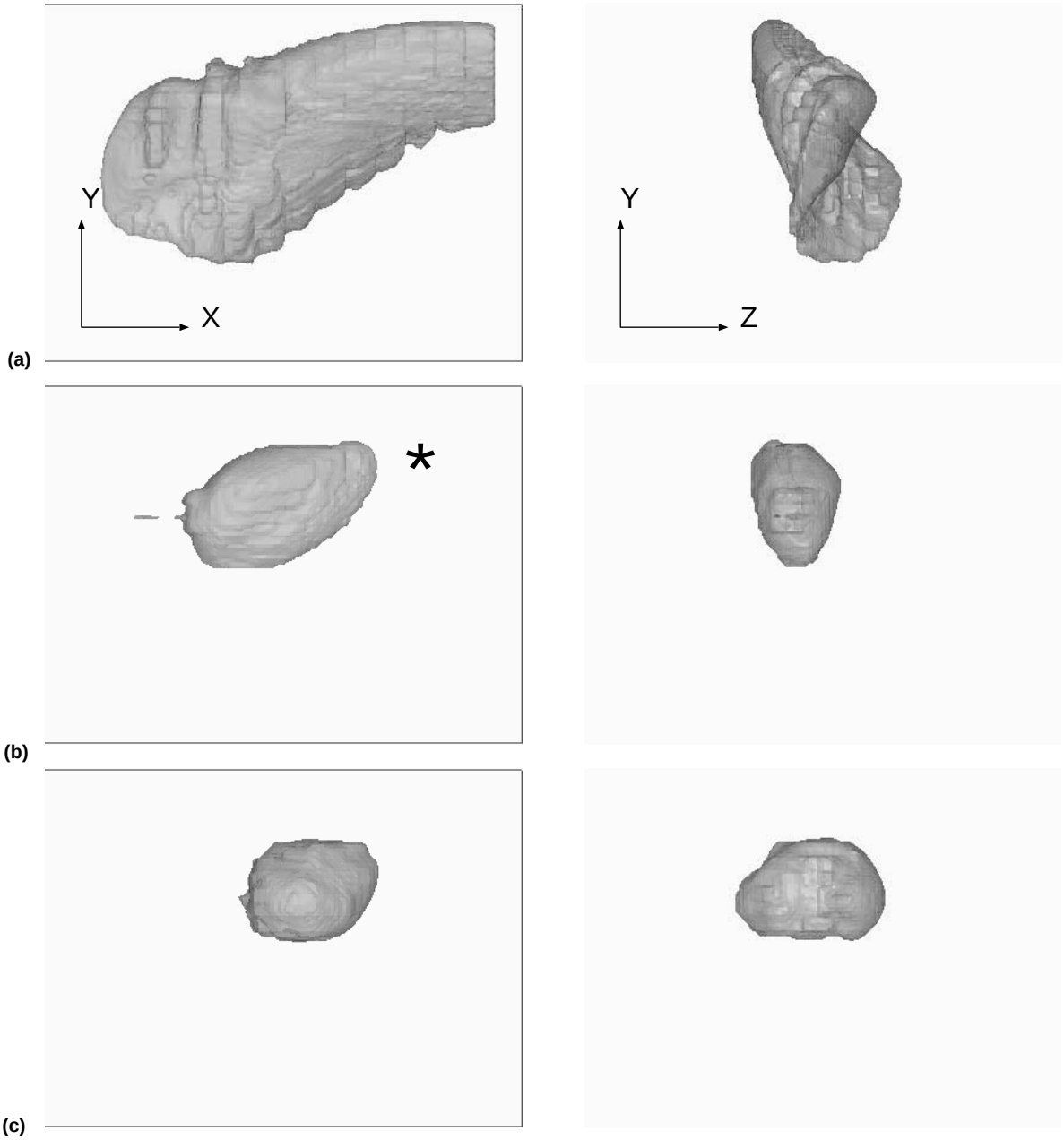

Fig. 8. Deformation of droplet (a) fluid element, (b) high-viscosity droplet without interfacial tension, (c) high-viscosity droplet with interfacial tension.

coefficient, and the viscous stress of the fluid, respectively. The viscous coefficient varies in space with the phases. f_i $(i = 1, 2, 3)$ represent the external body force per unit volume due to the interfacial tension. The constant fluid density, ρ, was set at unity.

Eq. (1) was solved by using the finite difference schemes of the staggered type and the fractional-step method (Kim and Moin, 1985). The velocity components were defined at the center of the cell surfaces, and the pressure and the external force were given at the center of the cell volume (hereafter, called grids). The second-order central difference scheme based on the interpolation method (Kawamura, 1995) and the second-order central difference scheme were applied for the finite-differencing of the convection and the viscous terms of Navier–Stokes equations, respectively. Poisson's equation for the pressure field was solved directly by using Fast Fourier Transforms (FFT) and Gaussian elimination (Schumann and Sweet, 1988). The third-order Runge–Kutta method (Rai and Moin, 1991) was used for the time-integration of the convective, viscous, and forcing terms in Eq. (1). The Courant number, Ct, based on the maximum axial velocity and the axial dimension of the original cell, Δx, peaked at 0.09. Thus, the Courant number, $\tilde{C}t$, based on the dimension of the fine cell mentioned below, $\Delta\tilde{x}$, was 0.72.

In the wall-normal direction, the non-slip boundary condition and the Neumann boundary condition were imposed for velocity components and the pressure, respectively. The periodical boundary conditions were given for both velocity components and the pressure in the x and z directions.

2.3. Modified VOF algorithm and local grid refinement

The position of the interface was determined by the fraction of the continuous-phase fluid, F, occupying a cell. $F = 1$ represents a cell filled with the fluid of the continuous-phase, while $F = 0$ indicates that the cell is filled with the fluid of the droplet. The cells of $0 < F < 1$ include the interface. The time evolution of F was estimated with the modified VOF algorithm (Hirt and Nichois, 1981), i.e., it was obtained by the convection equation as

$$\frac{\partial F}{\partial t} = -u_k \frac{\partial F}{\partial x_k}. \tag{3}$$

The second-order Adams–Bashforth method and the second-order central difference schemes were used for the time-integration and the spatial-differencing of Eq. (3), respectively. In order to obtain more points near the interface and to approximate the interface more locally and precisely, the local grid refinement (Tanaka et al., 1997) was adopted. In this technique, each original cell near the interface is further divided into fine cubic cells of sides $\Delta\tilde{x} = \Delta x/8$. The points on the interface were calculated for fine cells which contain the interface by using the values of F. Eq. (3) was discretized on these fine grids. The values of the velocity components at the fine grids, required for solving Eq. (3), were estimated firstly by linear interpolation of the velocity components of the original cells, and then the estimated velocity was corrected so that the equation of continuity was satisfied for each fine cell at any time step. The local grid refinement was also effective for reducing the numerical diffusion of F. The slope of the interface was also taken into account (Shirakawa et al., 1996).

2.4. Viscous coefficient

In order to evaluate the viscous term in the Navier–Stokes equation (the fourth term in Eq. (1)), the value of the viscous coefficient is needed at the volume center ($\boldsymbol{x}_a$) or the centers of the sides ($\boldsymbol{x}_b$) of the cell, depending on the special derivatives $\partial u_i/\partial x_j + \partial u_j/\partial x_i$ whether $i = j$ or $i \neq j$, respectively. It was evaluated as

$$\mu(\boldsymbol{x}) = \bar{F}(\boldsymbol{x})\mu_c + (1 - \bar{F}(\boldsymbol{x}))\mu_d, \tag{4}$$

where μ_c and μ_d are the viscous coefficients for the continuous and dispersed phases, respectively, and $\bar{F}$ is the average of F over the domain whose dimension is the same as the original cell and whose center is located at $\boldsymbol{x} = \boldsymbol{x}_a$ or $\boldsymbol{x}_b$ (the box drawn by the solid lines and that by the broken lines in Fig. 2, respectively). Consistent application of evaluation of the viscous coefficient near the interface may give high accuracy for the calculation of the viscous term.

2.5. Interfacial tension

The interfacial tension was calculated by the following procedure. Let $N_m (m = 1, 2, \ldots, M)$ be the points of intersections between the spherical surface, which approximates

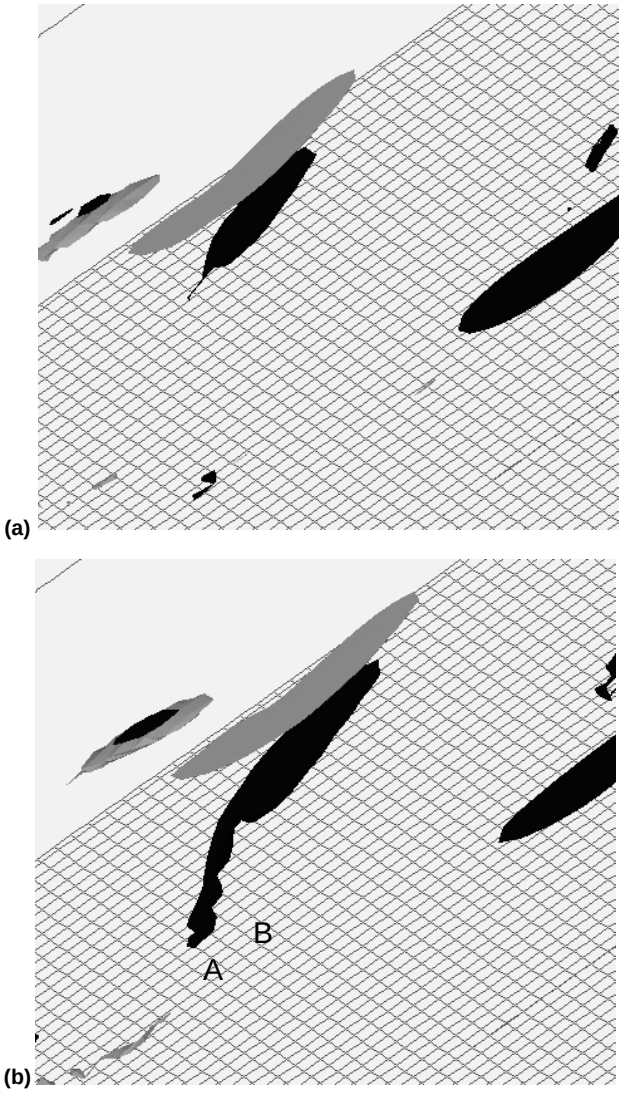

Fig. 9. Regions of high streamwise voriticity in the case without the droplet: (a) $t^* = 3$, (b) $t^* = 4$.

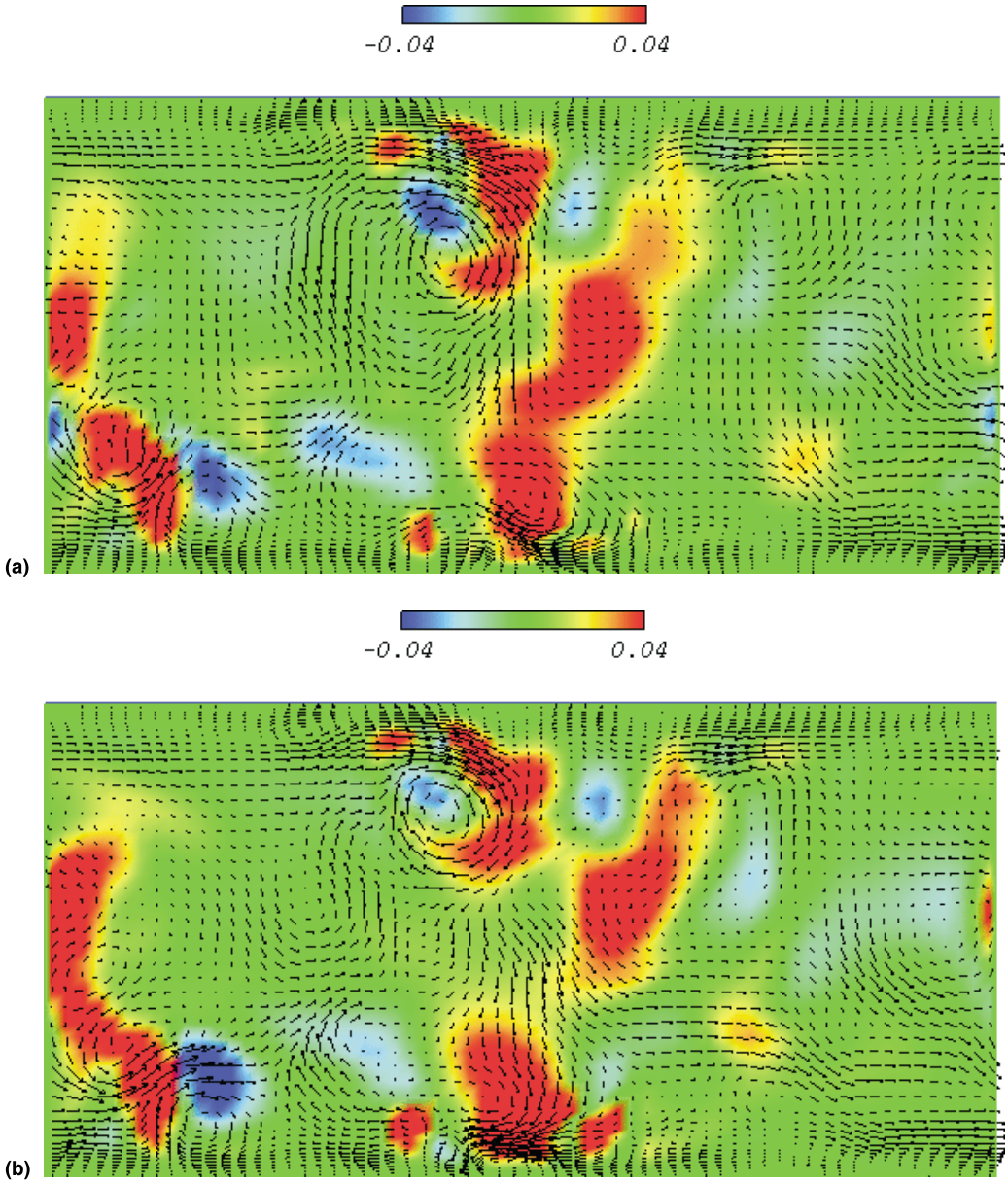

Fig. 10. Velocity distribution and color contour map of the difference between the Reynolds-shear stress product and the Reynolds shear stress in the (y,z)-planes with the cross-section of the droplet (fluid element): (a) $x/h=-1.4$ (A in Fig. 9(b)), (b) $x/h=-1.1$ (B in Fig. 9(b)).

the interface, and the sides of the original cell (see Fig. 3). Here, the unit vector normal to the interface, $\boldsymbol{n}$, was estimated as

$$\boldsymbol{n}=\frac{\sum_{m=1}^{M}\boldsymbol{n}_m}{\left|\sum_{m=1}^{M}\boldsymbol{n}_m\right|},$$

where $\boldsymbol{n}_m=\vec{CN}_m$ $(m=1,2,\ldots,M)$ and C denotes the center of the sphere. The area of the spherical surface was approximated by the sum of those of triangles which consist of the points $N_m(m=1,2,\ldots,M)$, and the point of intersection between the spherical surface and the normal vector.

Using the interface area S and the radius R of the sphere obtained above, the external body force in Eq. (1) was calculated as

$$f\{\Delta x\Delta y(y)\Delta z\}=\sigma\left(\frac{1}{R_1}+\frac{1}{R_2}\right)S(-\boldsymbol{n})=\sigma\frac{2}{R}S(-\boldsymbol{n}), \tag{5}$$

where σ is the coefficient of the interfacial tension.

2.6. Computational condition for droplet

We have introduced the droplet with diameter of $4\Delta x(=32\Delta\tilde{x}=41.3\nu/u_\tau)$ into near-wall turbulence. Computations have been performed for three different values of the viscosity μ_c/μ_d and the interfacial tension $\sigma^*(=\sigma/\rho U_W^2 h)$ of the droplet; (a) the fluid element $(\mu_d/\mu_c=1,\sigma^*=0)$, (b) the viscous droplet without interfacial tension $(\mu_d/\mu_c=40,\sigma^*=0)$, and (c) the viscous droplet with interfacial tension $(\mu_d/\mu_c=40,\sigma^*=1.0\times10^{-2})$. Since the introduction of the

droplet with high interfacial tension causes inconsistency of local turbulent flow field, particularly just after the introduction in the computation, the interfacial tension in case (c) was kept low. Then, the effect of the introduction of the droplet on the main flow was not serious because the ratio of the surface tension energy at the initial, K_s, to the kinetic energy of the carrier fluid flow per unit mass, K_f, was at highest 0.0625 locally. Therefore, the effect of the droplet on the whole flow field was negligibly small.

The initial velocity field for the three cases was identical. The initial position of the center of the droplet was (−1.5, 0.5, −0.5), and identical for the three cases.

3. Results and discussion

3.1. Turbulence statistics in the case without the droplet

The mean velocity and the turbulence intensities in the case without droplets were calculated from the ensemble averages over space and time for $1250h/U_W(6560\nu/u_\tau^2)$ after the statistically stable state was confirmed. The profiles of the mean velocity and the turbulence intensities are shown in Figs. 4 and 5, respectively. For comparison, we also show the experimental results measured by Bech et al. (1995) at the Reynolds number of $Re^* = 1260$, those measured by Aydin and Leutheusser (1987, 1991) at $Re^* = 1300$ and the numerical results obtained by Bech et al. (1995) at $Re^* = 1300$. The present computational results show fairly good agreement with the experimental data except u'_{rms} in the core region. Higher values of u'_{rms} and lower values of v'_{rms} than those measured or predicted (Bech et al., 1995) are observed in the present results. The identical discrepancy is also found in the computational results of Lee and Kim (1991), and Papavassiliou and Hanratty (1997). It is considered for the reason of this discrepancy that very-large-scale eddies (Bech and Andersson, 1994) contributing to the redistribution of the turbulence are not predicted properly because of the periodical boundary condition and the small computational domain. However, the boundary condition and the domain do not exert serious influence on the prediction of the developing small-scale streamwise vortices.

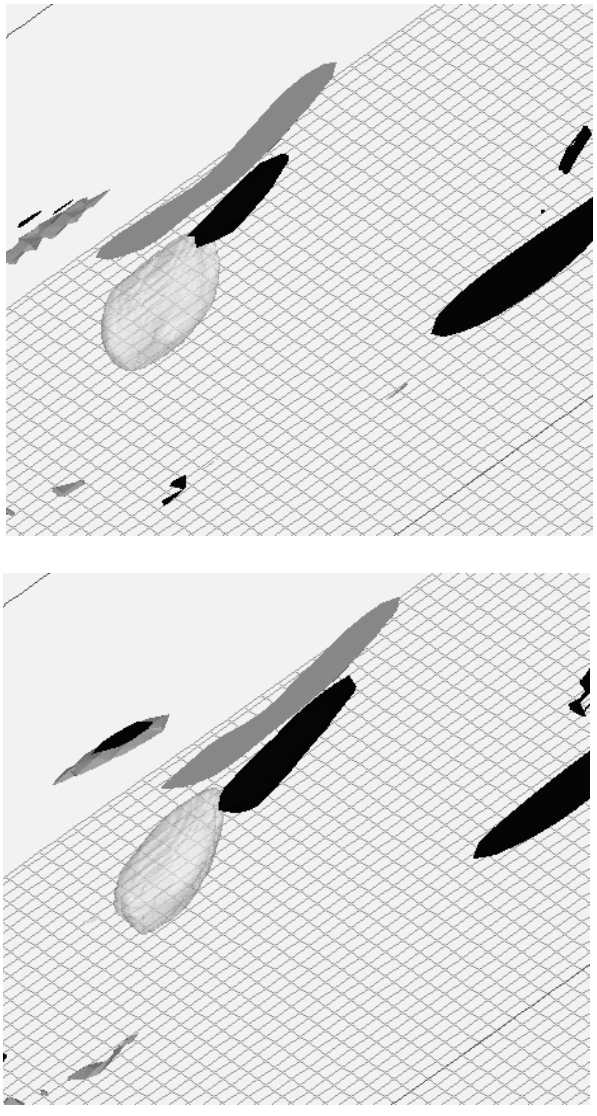

Fig. 11. Regions of high streamwise voriticity in the case with the droplet without the interfacial tension: (a) $t^* = 3$, (b) $t^* = 4$.

3.2. Time change in droplet volume

Fig. 6 demonstrates the time change in the droplet volume for the interval of $6h/U_W(= 31.5/\nu u_\tau^2)$. The volume was defined as the sum of the values of $(1 - F)$ for each fine cell. The volume of fluid lump increases rapidly with time due to the numerical diffusion. The volume of high-viscosity droplet without the interfacial tension is found to increase more gradually than the fluid lump. The numerical diffusion was attenuated by the high viscosity. The conservation of the volume of high-viscosity droplet with the interfacial tension is satisfactory throughout the interval. We found that the small-scale deformation of the interface, which may cause the numerical diffusion, becomes noticeable after $t^*(= tU_W/h) = 4$. Since the period of $4h/U_W$ is estimated to be comparable to that of the development of small-scale coherent structures, we focus on the phase interaction for the period.

3.3. Secondary flow along the interface

Fig. 7 shows a snapshot of the velocity field on an (x, y)-plane near the center of the droplet with interfacial tension at $t^* = 4$. Light grey region in this figure represents the droplet. Secondary flow in the wall-normal direction is found on both sides of the droplet. Similar secondary flow was observed experimentally for the oil droplet with higher interfacial tension ($\mu_d/\mu_c = 20, \sigma^* = 4.0$ or 5.5×10^{-2}) at the center of the turbulent Couette water flow (Hagiwara et al., 1998, 2000). It is shown from Figs. 6 and 7 that the droplet with interfacial tension can be predicted for the period of $4h/U_W$.

3.4. Deformation of the droplet

The droplet shapes at $t^* = 4$ are drawn in Fig. 8 for (a) the fluid element, (b) the viscous droplet without interfacial tension, and (c) the viscous droplet with interfacial tension. In these figures the upper (lower) wall is moving in the right (left) direction. Fig. 8(a) shows that the fluid element is highly deformed by the mean velocity of the surrounding fluid and the numerical diffusion. By comparing Fig. 8(b) with Fig. 8(a), we can see that the high-viscosity droplet is still elongated in the x direction and squeezed in the z direction but less deformed than the fluid element, which indicates that the high viscosity of the droplet suppresses the

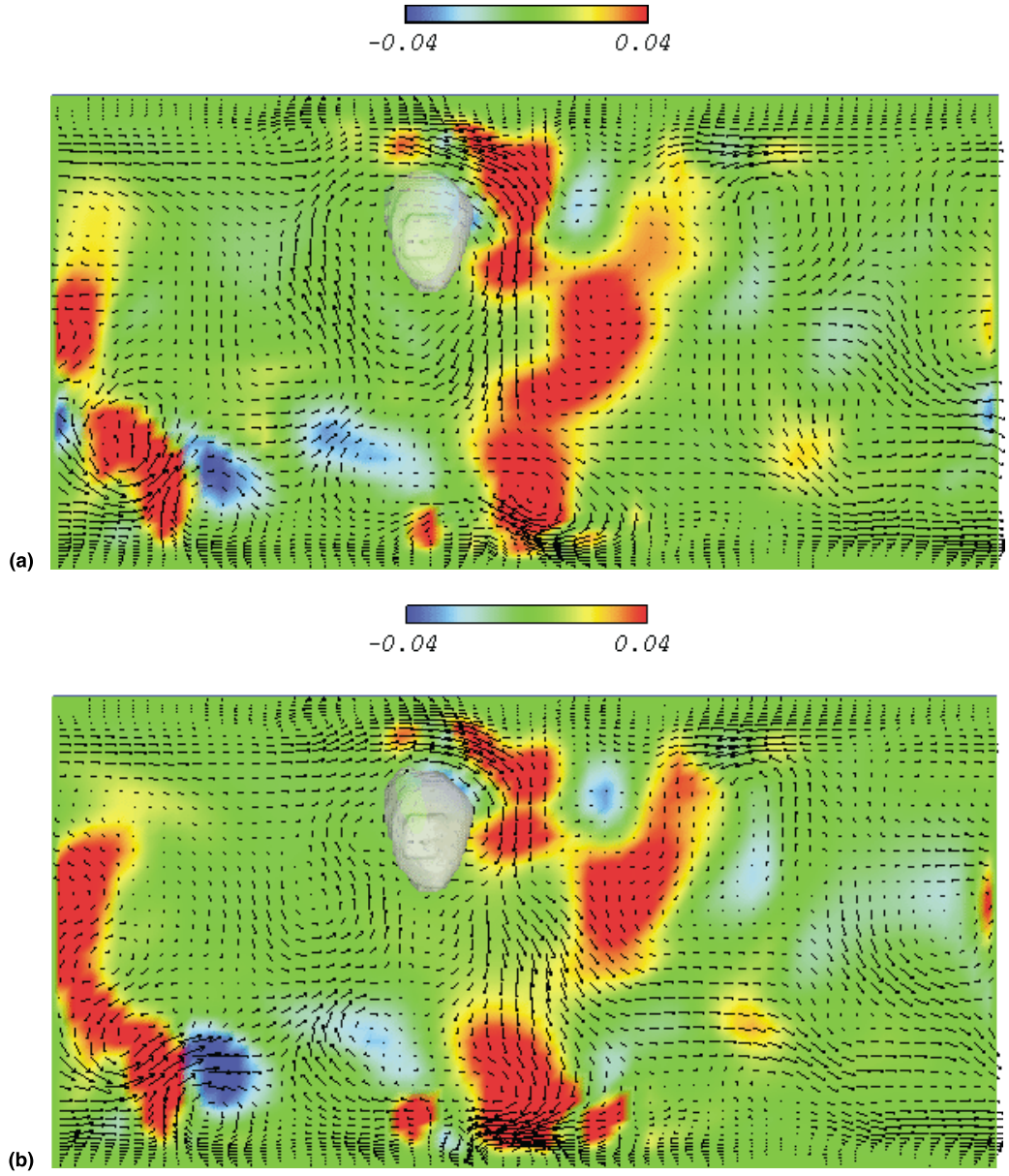

Fig. 12. Velocity distribution and color contour map of the difference between the Reynolds-shear stress product and the Reynolds shear stress in the (y,z)-planes with the cross-section of the viscous droplet without the interfacial tension: (a) $x/h = -1.4$, (b) $x/h = -1.1$.

deformation of the droplet. In contrast with these two types of droplets, the high-viscosity droplet with interfacial tension is neither elongated nor squeezed in Fig. 8(c). It seems that the local deformation of the droplet seen in Figs. 8(a) and (b) is attenuated by the restoration force due to the interfacial tension acting on the part of the droplet (marked *) where the interfacial curvature is large. In summary, the deformation of the droplet caused by the surrounding carrier fluid is particularly suppressed by the interfacial tension of the droplet.

3.5. Interaction between the droplet and streamwise vortices

We extracted near-wall coherent structures from the turbulent Couette flow as regions of high streamwise vorticity ω_x. Dark grey and black regions shown in Fig. 9 represent those of $\omega_x^* = \omega_x h/U_W = -2.0$ and $\omega_x^* = 2.0$, respectively. The transparent upper (tiled lower) wall is moving in the upper-right (lower-left) direction in the figure. The black region near the center of each figure can be regarded as a streamwise vortex since it was also captured by the vortex-identification method proposed by Jeong et al. (1997). It was found from the successive computational results that this streamwise vortex was generated at about $t^* = 1$ and developed as time proceeded: the leg extended to the downstream ($t^* = 3$) and the head extended to the upstream and to the axis ($t^* = 4$).

Fig. 10 demonstrates the velocity field in two adjacent (y,z)-planes at the same instant as that in Fig. 9. Clockwise fluid motion is clearly seen in the upper part of each figure, which is due to the streamwise vortex drawn in black in Fig. 9. Since this vortical motion is strong, the fluid element had been elongated downward. Fig. 10 also indicates the color

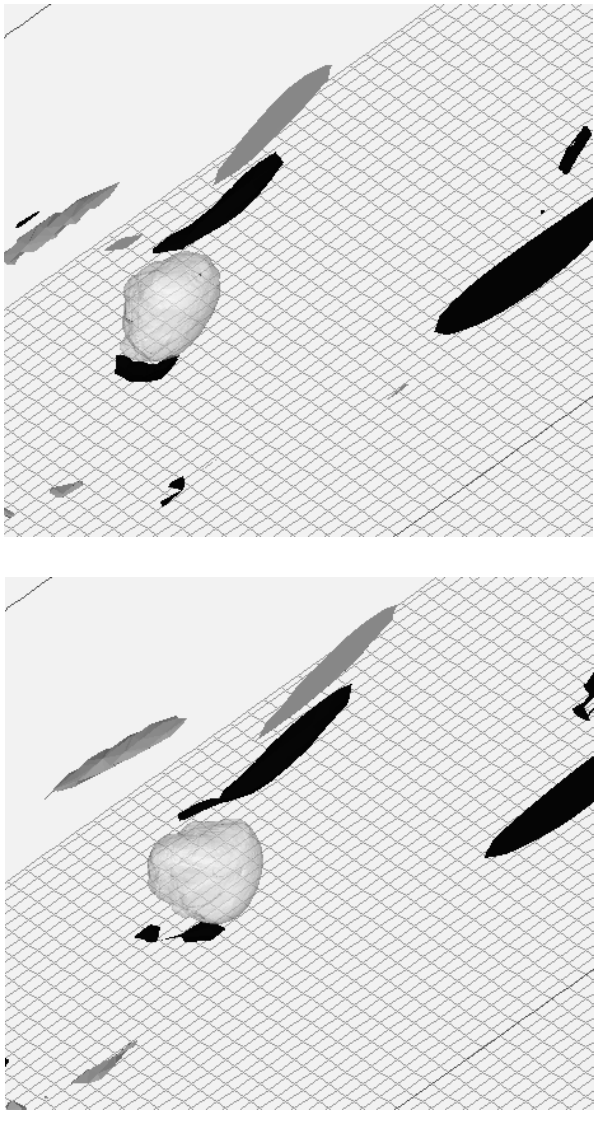

Fig. 13. Regions of high streamwise voriticity in the case with the droplet with the interfacial tension: (a) $t^* = 3$, (b) $t^* = 4$.

contour map of the difference between the instantaneous Reynolds-shear stress product and the Reynolds shear stress, $[-u'v' - (-\overline{u'v'})]/U_W^2$. Red and yellow show positive value of the difference, while blue and dark blue show negative values. The higher values of the product than its spaciotemporal average, which may contribute to the production of turbulence, are found in a region in the downward flow by the fluid motion. This is because fluid lump with high streamwise velocity ($+u'$) near the moving wall is transported into the core region of low streamwise velocity with high downward velocity ($-v'$). Similar regions are seen in the central part of this figure. These were caused by the other streamwise vortices, which had already been developed. By comparing the size and the wall-normal location of these regions, the streamwise vortex in the upper part of the figures is found to be still developing.

Fig. 11 shows the high-vorticity regions in the case with the high-viscosity droplet without interfacial tension. Light grey region represents the droplet. Comparing Fig. 11 with Fig. 9, we notice that the streamwise vortex (the black region of $\omega_x^* = 2.0$) near the droplet is shorter than that without the droplet at $t^* = 3$. This indicates the interaction between the droplet and the streamwise vortex. Then, the evolution of the head of the streamwise vortex was attenuated by the droplet at $t^* = 4$.

Fig. 12 demonstrates the velocity distribution in the same (y, z)-planes as those in Fig. 10 with the cross-section of the high-viscosity droplet. The higher region of Reynolds-shear stress product than its average does not change noticeably by the existence of the high-viscosity droplet. On the other hand, the downward fluid motion is enhanced near the lower part of the droplet in Fig. 12(b) because the fluid in the motion cannot penetrate the droplets.

In Fig. 13, the regions of $\omega_x^* = 2.0$ and $\omega_x^* = -2.0$ are plotted for the case with a high-viscosity droplet with the interfacial tension. The vorticity field near the droplet is much different from that in the other two cases: Two small vortices with positive vorticity are seen near the droplet in the figure. The longer one is the streamwise vortex, which is highly attenuated by the droplet. The smaller one is found to be induced by the droplet. This is related to the wake flow of the droplet. Judging from the velocity field shown in Fig. 7, the velocity difference across the interface is more noticeable at the lower part of the droplet than that at the top of the droplet. This is consistent with the smaller region of high vorticity.

Fig. 14 demonstrates the velocity distribution in the same (y,z)-planes as those in Fig. 10 with the cross-section of the high-viscosity droplet with interfacial tension. The fluid motion along the right-hand side of the droplet in Fig. 14(a) is not circulating but translational. Furthermore, not vortical motion but only small-scale velocity fluctuations are seen in Fig. 14(b). The color contour shows that the regions of higher values for the product than the average near the upper wall are much more localized compared with those in Figs. 10 and 12. On the other hand, the regions in the central part of the figure become larger than those in Figs. 10 and 12. These are due to the translational fluid motion. It is obtained from the computational data that these interactions continue for long time in the period examined. We expect that this kind of gradual, long-lasting interaction may cause a change in statistical quantities, such as a decrease in the wall shear stress, i.e., drag reduction.

4. Conclusions

We have conducted the direct numerical simulation of a liquid turbulent Couette flow with immiscible droplets. The main conclusions obtained are as follows.

1. A droplet in a turbulent Couette flow is deformed locally by the carrier fluid flow, but the deformation is particularly suppressed by the effect of the interfacial tension of the droplet.
2. Near-wall streamwise vortex is attenuated by the existence of the droplet with the interfacial tension.
3. The small vortex is generated in the wake region of the droplet.
4. The Reynolds-shear stress product becomes higher in a wide region around the droplet. This is due to the translational flow induced by the droplet.

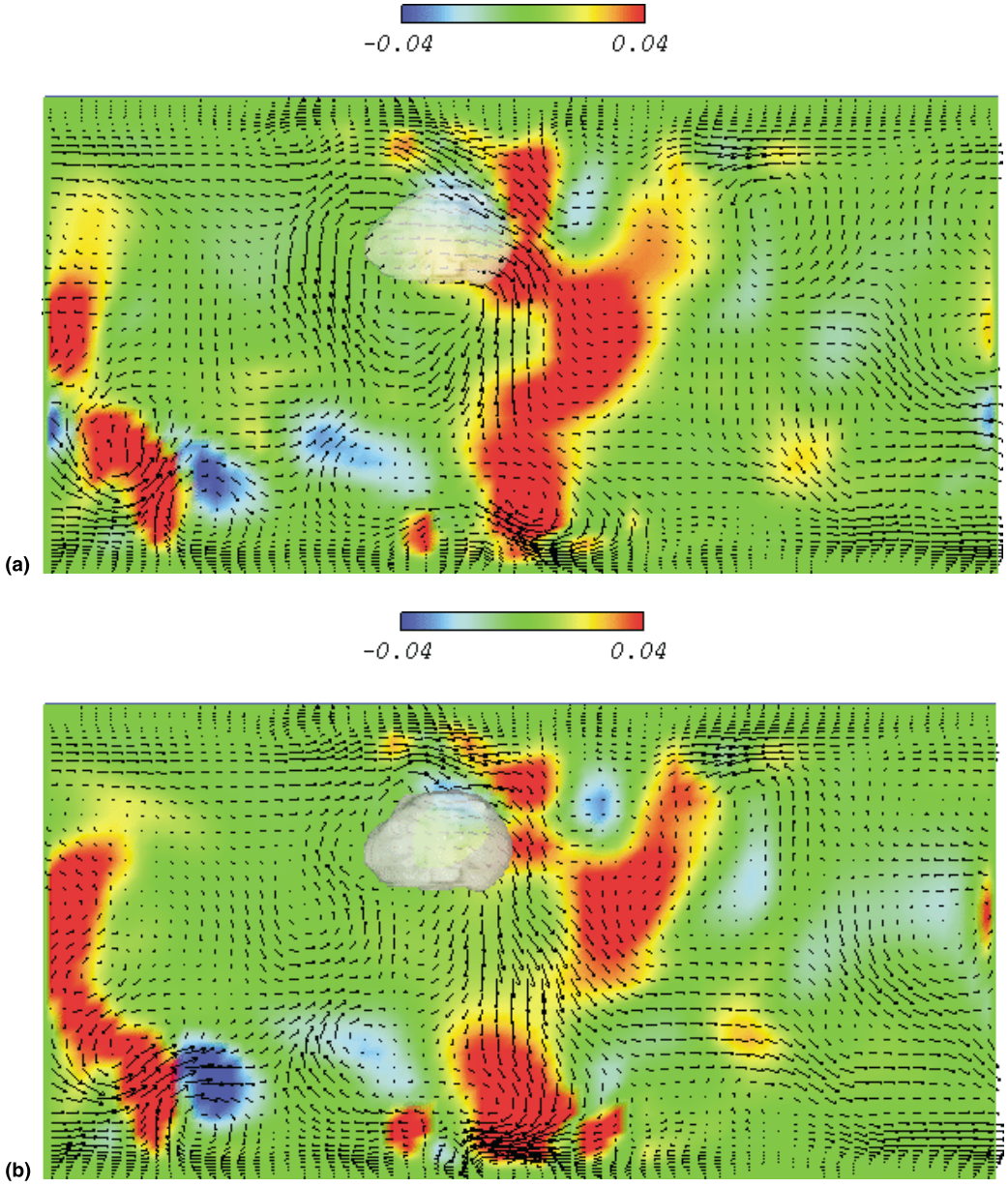

Fig. 14. Velocity distribution and color contour map of the difference between the Reynolds-shear stress product and the Reynolds shear stress in the (y,z)-planes with the cross-section of the viscous droplet with the interfacial tension: (a) $x/h = -1.4$, (b) $x/h = -1.1$.

References

Angeli, P., Hewitt, G.F., 1998. Pressure gradient in horizontal liquid-liquid flows. Int. J. Multiphase Flow 24, 1183–1203.

Aydin, E.M., Leutheusser, H.J., 1987. Experimental investigation of turbulent plane-Coette flow. In: Bower, W.W. (Ed.), Forum on Turbulent Flows, vol. 51. ASME FED, pp. 51–54.

Aydin, E.M., Leutheusser, H.J., 1991. Plane-Coette flow between smooth and rough walls. Exp. Fluids 11, 302–309.

Bech, K.H., Tillmark, N., Alfredsson, P.H., Andersson, H.I., 1995. An investigation of turbulent plane Couette flow at low Reynolds number. J. Fluid Mech. 286, 291–325.

Bech, K.H., Andersson, H.I., 1994. Very-large-scale Structure in DNS. In: Voke, P.R., Kleiser, L., Chollet, J.-P. (Eds.), Direct and Large-eddy Simulation I. Kluwer Academic Publisher, Dordrecht, MA, pp. 13–24.

Brackbill, J.U., Kothe, D.B., Zemach, C., 1992. A continuum method for modeling surface tension. J. Comput. Phys. 100, 335–354.

Hagiwara, Y., Takashina, Y., Tanaka, M., Nishimura, K., 1997a. Direct numerical simulation of the basic phase-interactions in liquid turbulent channel flow with immiscible droplets. Nucl. Eng. Design 175, 49–57.

Hagiwara, Y., Takashina, Y., Tanaka, M., Nishimura, K., 1997b. Interaction between a relatively high-viscosity immiscible droplet and coherent structure in liquid turbulent Couette flow. Transport Phenomena in Thermal Science and Process Engineering 1, 55–60.

Hagiwara, Y., None, T., Tanaka, M., Nishino, M., 1998. Turbulence modification and interface deformation in turbulent liquid plane

Couette flow with an immiscible droplet. JSME Int. J. 41B (2), 486–492.

Hagiwara, Y., Nishino, M., Tanaka, M., Sakamoto, S., 2000. 3-D PTV measurement on turbulence modification due to an oil droplet in a plane Couette water flow. J. Visualization 3, 101–113.

Hamilton, J.M., Kim, J., Waleffe, F., 1995. Regeneration mechanisms of near-wall turbulence structures. J. Fluid Mech. 287, 317–348.

Hirt, C.W., Nichois, B.D., 1981. Volume of fluid method for the dynamics of free boundaries. J. Comput. Phys. 39, 201–225.

Jeong, J., Hussain, F., Schoppa, W., Kim, J., 1997. Coherent structures near the wall in a turbulent channel flow. J. Fluid Mech. 332, 185–214.

Kawamura, H., 1995. Direct numerical simulation of turbulence by finite difference scheme. In: The Recent Developments in Turbulence Research. International Academic Publishers, pp. 54–60.

Kim, J., Moin, P., 1985. Application of a fractional-step method to incompressible Navier–Stokes equations. J. Comput. Phys. 59, 308–323.

Lee, M.J., Kim, J., 1991. The structure of turbulence in simulated plane Couette flow. In: Proceedings of the Eighth Symposium on Turbulent Shear Flows, pp. 5.3.1–5.3.6.

Pal, R., 1993. Pipeline flow of unstable and surfactant-stabilised emulsions. AIChE J. 39, 1754–1764.

Osher, S., Sethian, J.A., 1988. Fronts propagating with curvature-dependent speed: algorithms based on Hamilton-Jacobi formulation. J. Comput. Phys. 79, 12–49.

Papavassiliou, D.V., Hanratty, T.J., 1997. Interpretation of large-scale structures observed in a turbulent plane Couette flow. Int. J. Heat Fluid Flow 18, 55–69.

Rai, M.M., Moin, P., 1991. Direct simulations of turbulent flow using finite-difference schemes. J. Comput. Phys. 96, 15–53.

Schumann, U., Sweet, R.A., 1988. Fast Fourier transforms for direct solution of Poisson's equation with staggered boundary conditions. J. Comput. Phys. 74, 123–137.

Shirakawa, H., Takata, Y., Kuroki, T., Ito, T., 1996. Improvement of donor-acceptor method and the calculation of surface tension force term in volume of fluid (VOF) method. Trans. Jpn Soc. Mech. Eng. 62, 4068–4076 in Japanese.

Tanaka, M., Takashina, Y., Hagiwara, Y., Nishimura, K., 1997. Evaluation in interaction between an immiscible droplet and a liquid laminar Couette flow using local mesh refinement. In: ISAC'97 High Performance Computing on Multiphase Flows, pp. 31–34.

Tomiyama, A., Sou, A., Zun, I., Kanami, N., Sakaguchi, T., 1995. Effects of Eötvös number and dimensionless liquid volumetric flux on lateral motion of a bubble in a laminar duct flow. In: Proceedings of the Second International Conference on Multiphase Flow '95 Kyoto, vol. 1, pp. PD1-11–PD1-18.

Unverdi, S.O., Tryggivason, G., 1992. A front-tracking method for viscous, incompressible, multi-fluid flows. J. Comput. Phys. 100, 25–37.